ACS OMEGA

http://pubs.acs.org/journal/acsodf

Article

Thermal Properties of 2D Dirac Materials MN_4 (M = Be and Mg): A First-Principles Study

Man Wang and Dan Han*

Cite This: *ACS Omega* 2022, 7, 10812−10819

Read Online

ACCESS | Metrics & More | Article Recommendations

ABSTRACT: Recently, a novel two-dimensional (2D) Dirac material BeN_4 monolayer has been fabricated experimentally through high-pressure synthesis. In this work, we investigate the thermal properties of a new class of 2D materials with a chemical formula of MN_4 (M = Be and Mg) using first-principles calculations. First, the cohesive energy and phonon dispersion curve confirm the dynamical stability of BeN_4 and MgN_4 monolayers. Besides, BeN_4 and MgN_4 monolayers have the anisotropic lattice thermal conductivities of 842.75 (615.97) W m^{-1} K^{-1} and 52.66 (21.76) W m^{-1} K^{-1} along the armchair (zigzag) direction, respectively. The main contribution of the lattice thermal conductivities of BeN_4 and MgN_4 monolayers are from the low frequency phonon branches. Moreover, the average phonon heat capacity, phonon group velocity, and phonon lifetime of BeN_4 monolayer are 3.54 × 10^5 J K^{-1} m^{-3}, 3.61 km s^{-1}, and 13.64 ps, which are larger than those of MgN_4 monolayer (3.42 × 10^5 J K^{-1} m^{-3}, 3.27 km s^{-1}, and 1.70 ps), indicating the larger lattice thermal conductivities of BeN_4 monolayer. Furthermore, the mode weighted accumulative Grüneisen parameters (MWGPs) of BeN_4 and MgN_4 monolayers are 2.84 and 5.62, which proves that MgN_4 monolayer has stronger phonon scattering. This investigation will enhance an understanding of thermal properties of MN_4 monolayers and drive the applications of MN_4 monolayers in nanoelectronic devices.

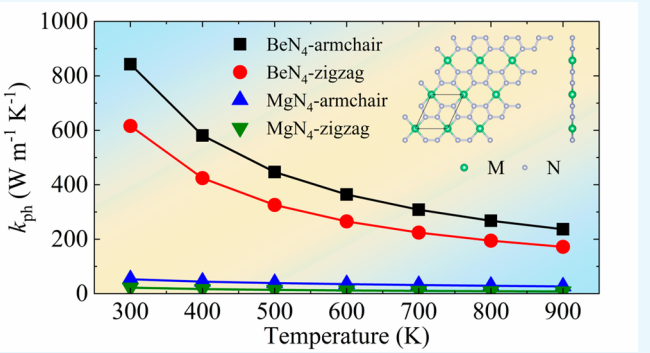

1. INTRODUCTION

The successful preparation of a one-atom-thick two-dimensional (2D) material graphene in 2004 breaks the conventional view that 2D crystal is regarded as an unstable structure in nature.[1] Meanwhile, graphene as a Dirac material has a feature of massless fermions, resulting in outstanding physical properties, such as ultrahigh carrier mobility,[2] half-integer/fractional/fractal quantum Hall effects,[3−5] high thermal conductivity,[6−8] large Young's modulus,[9] and other novel properties,[10] which has triggered a great deal of attention from researchers. On the other hand, graphene arouses the explorations of other hundreds of 2D materials, including graphene-like 2D materials (graphitic carbon nitride, hexagonal boron nitride, transition metal dichalcogenides, layered metal oxides, and layered double hydroxides), black phosphorus, silicene, antimonene, transition metal carbides and/or nitride, noble metals, metal−organic frameworks, covalent-organic frameworks, and so on.[11,12] However, in these materials, only silicene, germanene, stanene, tinene, graphynes (α-graphyne, β-graphyne, and 6,6,12-graphyne), rectangular carbon and boron allotropes (S-graphene, D-graphene, E-graphene, and *Pmmn* boron), and some other systems belong to 2D Dirac materials.[13−15] These 2D Dirac materials generally have spatial inversion symmetry and possess the advantages of quantum Hall effect, large Fermi velocity, and high carrier mobility,[15−17] making them a promising candidate for applications in nanoelectronic devices. Hence, there is the need to search the novel Dirac materials in the family of 2D materials.

Very recently, a novel nitrogen-rich Dirac material, beryllonitrene (BeN_4) monolayer has been synthesized successfully by employing high-pressure synthesis followed by decompression to ambient conditions.[18] It has been reported that BeN_4 monolayer belongs to a Dirac semimetal, and the electronic band structure near the Fermi energy exhibits the linear dispersion with two overlapped Dirac points, which is similar to graphene monolayer. However, unlike graphene monolayer, BeN_4 monolayer is an oblique crystal system with a lower symmetry, which leads to the fact that the Dirac points are located at the Σ point along the Γ-A direction in the Brillouin zone. Besides, BeN_4 monolayer has essentially

Received: February 8, 2022
Accepted: March 2, 2022
Published: March 14, 2022

anisotropic massless Dirac fermions and Fermi velocities (8×10^5 m s^{-1} along the Σ-Γ direction and 3×10^5 m s^{-1} along the Σ-A direction).[18] These outstanding electronic properties suggest that BeN_4 monolayer can be widely used in nanoelectronic devices. Apart from BeN_4 monolayer, another nitrogen-rich Dirac material, MgN_4 monolayer, belonging to the same class of MN_4 (M = Be and Mg) monolayers is examined by first-principles calculations.[19] Mortazavi et al. investigated the stability and the electronic nature of MN_4 monolayers and proved that the melting points of two monolayers were over 1000 K. Meanwhile, the corresponding tensile strengths of BeN_4 and MgN_4 monolayers were 100(43) and 74(39) GPa along the armchair (zigzag) direction, respectively. The corresponding elastic moduli were 946(590) and 582(353) GPa, indicating high lattice thermal conductivities of BeN_4 monolayer, which has been proven also in other work.[20] In practice, some materials with high lattice thermal conductivities are useful for enhancing the heat dissipation in miniaturized and high-power nanoelectronic devices, which plays a fundamental role in thermal management. Therefore, it is crucial to investigate the lattice thermal conductivity in BeN_4 and MgN_4 monolayers. However, to our knowledge, the thermal properties of BeN_4 and MgN_4 monolayers are yet to be broadly investigated. Hence, in the present work, we identify the lattice thermal conductivities and phonon behaviors of MN_4 monolayers.

In this work, the thermal properties of BeN_4 and MgN_4 monolayers are investigated systematically by utilizing first-principles calculations. First, we calculate the cohesive energies and phonon dispersion curves of BeN_4 and MgN_4 monolayers to demonstrate the dynamical stabilities. Moreover, the lattice thermal conductivities of BeN_4 and MgN_4 monolayers and phonon contributions are calculated. Furthermore, the phonon behaviors including the phonon heat capacity, the phonon group velocity, the phonon lifetime, the phonon mean free path (MFP), and the cumulative lattice thermal conductivity are studied. Especially, the mode weighted accumulative Grüneisen parameter (MWGP) and the phonon scattering phase space (P_3) are applied to interpret the strength and number of phonon scattering channels. Our investigation can provide deep insights into thermal properties of MN_4 monolayers.

2. METHODOLOGY

In this investigation, all calculations are carried out by the Vienna Ab initio Simulation Package (VASP) within the framework of density functional theory (DFT).[21] The electron−ion interaction is described by the projector augmented wave (PAW) method, and the generalized gradient approximation (GGA) of Perdew−Burke−Ernzerhof (PBE) is used to model the exchange-correlation functional.[22] For both monolayers, we set an energy cutoff for the plane waves to 500 eV. During the structure optimization, the Hellman-Feynman force and energy drops are lower than 10^{-3} eV Å^{-1} and 10^{-6} eV with a 15 × 13 × 1 Monkhorst−Pack k-point mesh, respectively. Meanwhile, a vacuum thickness of 20 Å along the z direction is applied to avoid interactions between the periodic images.

Thermal properties of BeN_4 and MgN_4 monolayers can be studied by utilizing the ShengBTE package,[23] which is widely used in the investigation of thermal properties of 2D materials (As_2Te_3, WS_2, WSe_2, and AlP_3).[24−26] After solving iteratively the Boltzmann transport equation (BTE), the lattice thermal conductivity can be expressed by the following formula:[27]

$$k_{\mathrm{ph}}^{\alpha\alpha} = \sum_{\lambda} C_{\lambda} v_{\lambda\alpha}^2 \tau_{\lambda} \tag{1}$$

where λ means phonon branch, α represents the Cartesian direction (x, y, and z), C_λ is the phonon heat capacity, $v_{\lambda\alpha}$ and $\tau_{\lambda\alpha}$ are the phonon group velocity and phonon lifetime, respectively. The phonon heat capacity C_λ can be given by:

$$C_{\lambda} = \frac{k_{\mathrm{B}}}{NV} \frac{(\hbar\omega_{\lambda}/k_{\mathrm{B}}T)^2 e^{\hbar\omega_{\lambda}/k_{\mathrm{B}}T}}{(e^{\hbar\omega_{\lambda}/k_{\mathrm{B}}T} - 1)^2} \tag{2}$$

where N is the total number of q points in a discretization of Brillouin zone, V means the system volume, ω_λ represents the phonon angular frequency, and T is the temperature. The parameters of k_B and $\hbar$ are the Boltzmann constant and reduced Planck constant, which are the physical constants. The phonon group velocity $v_{\lambda\alpha}$ can be obtained from the following expression:

$$v_{\lambda\alpha} = \partial\omega_{\lambda}/\partial q_{\alpha} \tag{3}$$

where q is the wave vector. The phonon lifetime τ_λ describing the three-phonon processes can be calculated by using the following formula:

$$\frac{1}{\tau_{\lambda}} = \frac{1}{N}\left(\sum_{\lambda'\lambda''} W_{\lambda\lambda'\lambda''}^{+} + \frac{1}{2}\sum_{\lambda'\lambda''} W_{\lambda\lambda'\lambda''}^{-}\right) \tag{4}$$

where W^+ and W^- are three-phonon scattering rates during the absorption and emission processes of phonons, respectively.[23]

The ShengBTE package requires interatomic force constants (IFCs) as input files. The second order and third order interatomic force constants (IFCs) are obtained by using DFT calculations, which are also known as harmonic and anharmonic IFCs. For harmonic IFCs, the dynamical matrix is calculated by using the density functional perturbation theory (DFPT).[28] The phonon harmonic properties can be extracted using Phonopy package with a 3 × 3 × 1 supercell and a 5 × 4 × 1 q mesh.[29] The anharmonic IFCs are obtained by using the thirdorder.py script with the same 3 × 3 × 1 supercell and 5 × 4× 1 q mesh.[23] Herein, we consider the interaction cutoff up to ten-nearest-neighbor atoms. Meanwhile, a long-range correction is introduced by calculating the Born effective charge and dielectric tensor, and the isotope scattering has been considered in the calculation of lattice thermal conductivity. A q point grid of 100 × 100 × 1 is selected to study the lattice thermal conductivity. Both thicknesses of BeN_4 and MgN_4 monolayers are set to 3.06 Å.[18]

3. RESULTS AND DISCUSSION

3.1. Crystal Features and Dynamic Stabilities of MN_4 Monolayers. In this section, we first optimize the MN_4 monolayers and measure the crystal features. As shown in Figure 1, the honeycomb-like monolayers exhibit the space group of $P2/m$ (No. 10) and point group of C2h. In both monolayers, each M atom is connected with four N atoms, and each N atom is connected with one M atom and two N atoms. For BeN_4 monolayer, the lattice constants of a = 3.66 Å and b = 4.27 Å, and the angle (γ) between in-plane lattice vectors is 64.63°. The corresponding values of MgN_4 monolayer are 3.86 Å, 4.88 Å, and 66.69°. These results are in agreement with other DFT results (BeN_4: 3.66 Å, 4.27 Å, and 64.64°; MgN4:

https://doi.org/10.1021/acsomega.2c00785
ACS Omega 2022, 7, 10812−10819

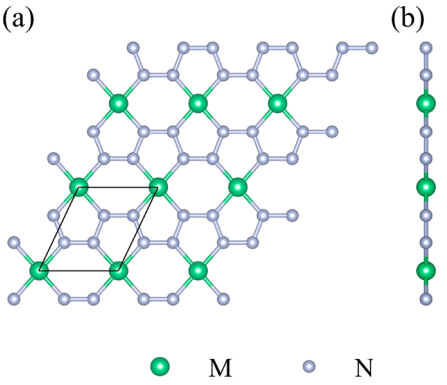

Figure 1. (a) Top and (b) side views of MN_4 monolayer. The solid line indicates the unit cell of MN_4 monolayer. The green spheres represent M (Be and Mg) atoms, and gray spheres represent N atoms.

3.86 Å, 4.88 Å, and 66.69°).[19] For BeN_4 monolayer, the two types of N−N bond lengths are found to be 1.343 and 1.338 Å, the Be−N bond length is determined to be 1.746 Å. For MgN_4 monolayer, three bond lengths are equal to 1.356 Å, 1.349 Å, and 2.055 Å, respectively. These data are consistent with that from previous work.[19,30] Besides, the electron localization functions (ELF) of two monolayers are calculated to further analyze the bonding nature. The ELF results with an isovalue of 0.7 are shown in Figure 2 and are similar to other DFT results.[19] ELF takes a value from 0 to 1 at each point. MN_4 monolayers consist of armchair-shaped polymeric nitrogen chains (N_∞). From Figure 2, we can observe that electrons are strongly localized on N_∞, and on each N pointing toward the M atoms. In BeN_4 and MgN_4 monolayers, the electron cloud of anionic N_∞ is strongly pulled to the Be and Mg atoms, which leads Be−N and Mg−N bonds to have higher covalent character. As shown in Figure 3, we obtain the electronic band structures of BeN_4 and MgN_4 monolayers by using the PBE functional. The electronic band structures of BeN_4 and MgN_4 monolayers are in good agreement with that from previous work,[19] indicating our DFT calculations are correct.

To evaluate the dynamic stability, we evaluate the cohesive energies and phonon dispersion curves of two monolayers. The cohesive energy can be calculated by the following expression: $E_{coh} = (E_M + 4 \times E_N - E_{MN4})/5$, in which E_M is the energy of an isolated M atom, E_N means the energy of an isolated N atom, and E_{MN4} represents the total energy of MN_4 monolayer. The calculated cohesive energies of BeN_4 and MgN_4 monolayers are 4.78 eV/atom and 4.32 eV/atom, respectively. The higher cohesive energy indicates a more stable structure, indicating that the BeN_4 monolayer has a more stable structure. The values of BeN_4 and MgN_4 monolayers are higher than those of phosphorene (3.3 eV/atom), GaP_3 (3.34 eV/atom), and InP_3 (3.19 eV/atom).[31,32] Moreover, the phonon dispersion curves of BeN_4 and MgN_4 monolayers are calculated to evaluate the dynamic stability, which is depicted in Figure 4. Unlike graphene monolayer, both Brillouin zone paths of two monolayers are along Γ-X-M-A-Y-Γ owing to the special monoclinic crystal. The atom numbers in MN_4 unit cells are five, leading to three acoustic phonon branches and 12 optical phonon branches. It can be observed from Figure 4 that at the Γ point, the transverse acoustic (TA) and longitudinal acoustic (LA) phonon branches exhibit linear relations, whereas the flexural acoustic (ZA) phonon branch has a parabolic relation. This phenomenon is also reported in other 2D materials.[33−35] Furthermore, the phonon dispersion curves of BeN_4 and MgN_4 monolayers are free of imaginary frequencies, which proves their dynamic stabilities. The cutoff frequency of optical phonon branches of BeN_4 and MgN_4 monolayers can reach up to 41.70 THz and 39.71 THz, which are higher than those of other 2D materials (silicene: ∼ 16.6 THz; WS_2: ∼ 13 THz; and WSe_2: ∼ 9 THz).[36−38] In addition, the acoustic phonon frequency region of BeN_4 monolayer is larger than that of MgN_4 monolayer, which gives rise to a larger phonon group velocity. It should be noted that for MN_4 monolayers, acoustic phonon branches are coupled with optical phonon branches. The couple region of MgN_4 monolayer (∼8 THz) is smaller than that of BeN_4 monolayer (∼12 THz), which promotes a stronger phonon scattering and a lower phonon lifetime. Hence, we can deduce that the order of lattice thermal conductivity is BeN_4 > MgN_4 (detailed interpretation can be found in the following section).

3.2. Lattice Thermal Conductivities of MN_4 Monolayers. Lattice thermal conductivities of BeN_4 and MgN_4 monolayers along the armchair (x) and zigzag (y) directions are shown in Figure 5. On one hand, it can be clearly seen that the thermal properties of BeN_4 and MgN_4 monolayers are anisotropic. For BeN_4 monolayer, at 300 K, the lattice thermal conductivities along the armchair and zigzag directions are equal to 842.75 W m^{-1} K^{-1} and 615.97 W m^{-1} K^{-1}, respectively. The corresponding values of MgN_4 monolayer are 52.66 W m^{-1} K^{-1} and 21.76 W m^{-1} K^{-1}. On the basis of our previous work, the isotropic lattice thermal conductivity of graphene at 300 K is 3544.41 W m^{-1} K^{-1}, which is much larger than the values of BeN_4 and MgN_4 monolayers.[39] On the other hand, high temperature will monotonically decline the lattice thermal conductivities of these monolayers. As the temperature

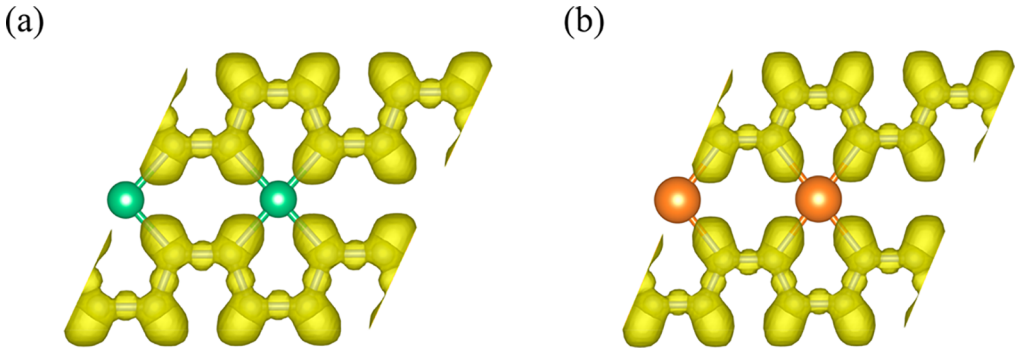

Figure 2. Isosurfaces of the electron localization function (ELF) calculated for (a) BeN_4 and (b) MgN_4 monolayers with an isovalue of 0.7.

https://doi.org/10.1021/acsomega.2c00785
ACS Omega 2022, 7, 10812−10819

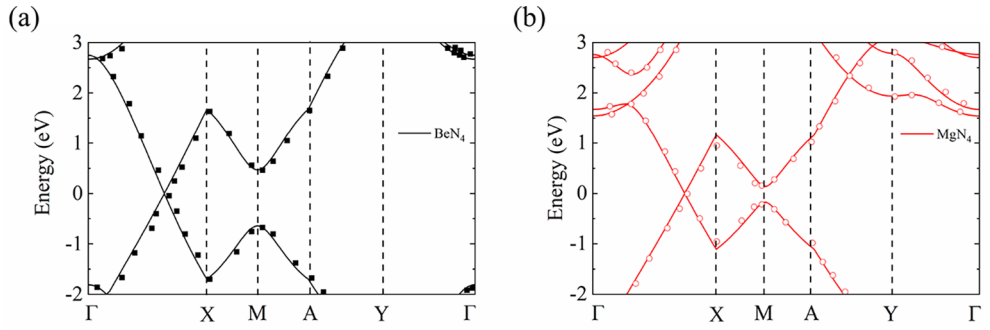

Figure 3. Electronic band structures of (a) BeN_4 and (b) MgN_4 monolayers. Black squares and red circles are from ref 19.

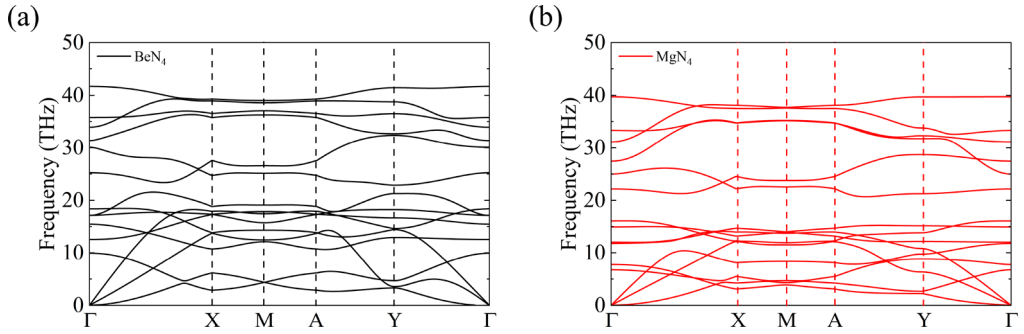

Figure 4. Phonon dispersion curves of (a) BeN_4 and (b) MgN_4 monolayers.

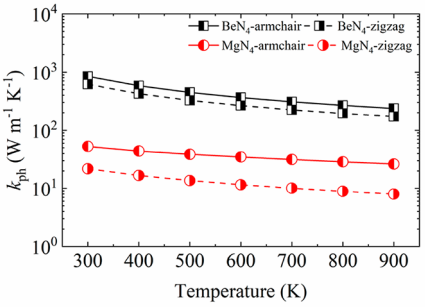

Figure 5. Lattice thermal conductivities of BeN_4 and MgN_4 monolayers along the armchair and zigzag directions as a function of the temperature.

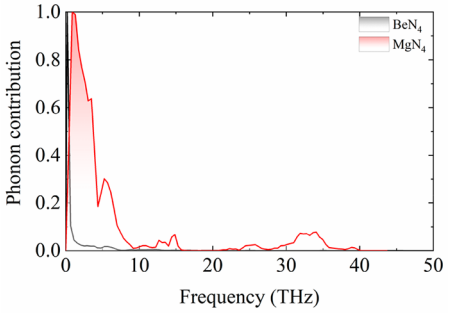

Figure 6. Phonon contributions to the total lattice thermal conductivities of BeN_4 and MgN_4 monolayers as a function of the frequency at 300 K.

increases from 300 to 900 K, the lattice thermal conductivities of BeN_4 and MgN_4 monolayers along the armchair and zigzag directions are reduced to 236.47 W m^{-1} K^{-1} and 171.66 W m^{-1} K^{-1}, 26.27 W m^{-1} K^{-1} and 7.96 W m^{-1} K^{-1}, respectively. The corresponding reductions are 71.94% and 72.13%, 50.11% and 63.43%, respectively. High temperature will activate high frequency phonons and strengthen the Umklapp phonon scattering, generating the lower lattice thermal conductivity. A similar trend can be observed in other 2D materials, such as transition metal dichalcogenide and triphosphides.[26,40] Additionally, we investigate the phonon contributions to the total lattice thermal conductivities of BeN_4 and MgN_4 monolayers, which is displayed in Figure 6. There are two facts that can be found in Figure 6: (1) For BeN_4 and MgN_4 monolayers, the contribution of low frequency phonons at 0−10 THz to the total lattice thermal conductivity is dominant. These low frequency phonons include the acoustic phonon branches and low frequency optical phonon branches. (2) The high frequency optical phonon branches have a small contribution to the total lattice thermal conductivities of BeN_4 and MgN_4 monolayers. This tendency has been proven in a previous study.[34]

3.3. Phonon Behaviors of MN_4 Monolayers. To gain a deeper understanding of thermal transport mechanism of BeN_4 and MgN_4 monolayers, the phonon behaviors are evaluated in this section, which includes the phonon heat capacity, the phonon group velocity, the phonon lifetime, the mode weighted accumulative Grüneisen parameter (MWGP), the phonon scattering phase space (P_3), the phonon mean free path (MFP), and the cumulative lattice thermal conductivity. We first calculate phonon heat capacities of BeN_4 and MgN_4 monolayers, which are equal to 3.54 × 10^5 J K^{-1} m^{-3} and 3.42 × 10^5 J K^{-1} m^{-3}, respectively. The higher phonon heat capacity of BeN_4 monolayer contributes to the larger lattice thermal conductivity in comparison with the MgN_4 monolayer. Besides, the phonon group velocities of BeN_4 and MgN_4 monolayers are obtained from the phonon dispersion curves in Figure 4. It can be obviously seen from Figure 7 that the phonon group velocity of BeN_4 monolayer is much larger than that of MgN_4 monolayer. In both BeN_4 and MgN_4 monolayers,

https://doi.org/10.1021/acsomega.2c00785
ACS Omega 2022, 7, 10812−10819

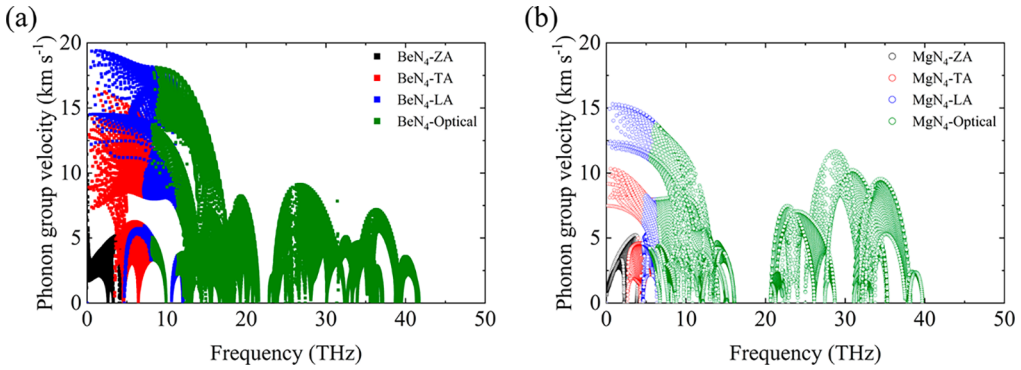

Figure 7. Phonon group velocities of (a) BeN_4 and (b) MgN_4 monolayers as a function of the frequency.

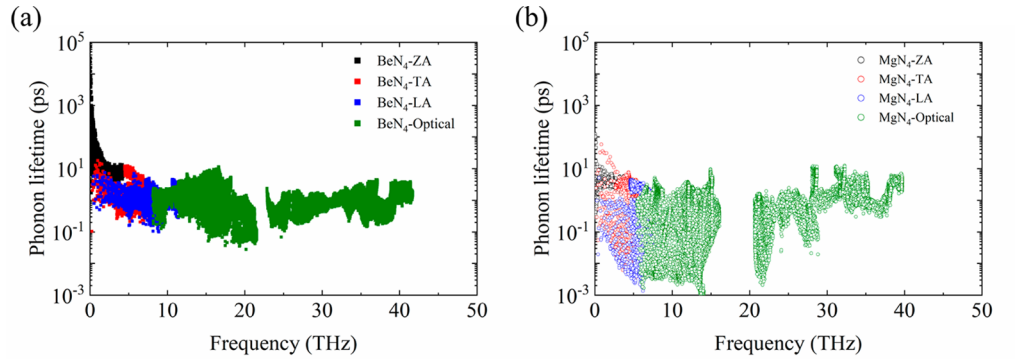

Figure 8. Phonon lifetimes of (a) BeN_4 and (b) MgN_4 monolayers as a function of the frequency.

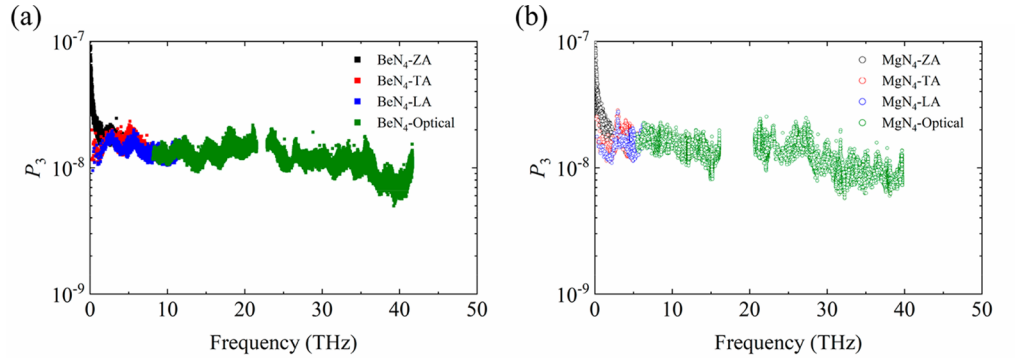

Figure 9. Phonon phase spaces (P_3) of (a) BeN_4 and (b) MgN_4 monolayers as a function of frequency at 300 K.

the LA phonon branches possess the largest phonon group velocity. Near the Γ point, for BeN_4 monolayer, the maximum phonon group velocities of TA and LA phonon branches are 16.77 km s^{-1} and 19.41 km s^{-1}, while the corresponding values of MgN_4 monolayer are 10.33 km s^{-1} and 15.30 km s^{-1}, respectively. For a more intuitive comparison, the average phonon group velocities of BeN_4 and MgN_4 monolayers are calculated, which are 3.61 km s^{-1} and 3.27 km s^{-1} in the whole frequency region, respectively, which are lower than that of graphene monolayer (7.09 km s^{-1}).[39] Particularly, the average phonon group velocities of high frequency phonons of BeN_4 and MgN_4 monolayers are 3.04 km s^{-1} and 2.89 km s^{-1}, which are smaller than the values of low frequency phonons (6.05 km s^{-1} and 4.16 km s^{-1}), indicating that the low frequency phonons have a large contribution to lattice thermal conductivity. According to eq 1, in comparison with MgN_4 monolayer, BeN_4 monolayer has a higher lattice thermal conductivity because of the higher phonon group velocity.

Apart from phonon heat capacity and phonon group velocity, phonon lifetime is another important factor that affects lattice thermal conductivity. The phonon lifetimes of BeN_4 and MgN_4 monolayers are plotted in Figure 8. For BeN_4 monolayer, the phonon lifetimes of acoustic phonon branches decline with the increasing phonon frequency, which are larger than those of optical phonon branches. This phenomenon can demonstrate that the high frequency optical phonon branches make a small contribution to lattice thermal conductivity. Besides, the ZA phonon branch has the largest phonon lifetime. However, for MgN_4 monolayer, the phonon lifetimes of acoustic phonon branches and optical phonon branches are in the same magnitude. It is noticed that the phonon lifetime of the TA phonon branch is slightly higher than those of other acoustic phonon branches. We can further observe from Figure 8 that the phonon lifetime of BeN_4 monolayer is much higher than that of MgN_4 monolayer, of which the average values are 13.64 and 1.70 ps, respectively. The larger phonon lifetime can

https://doi.org/10.1021/acsomega.2c00785
ACS Omega 2022, 7, 10812−10819

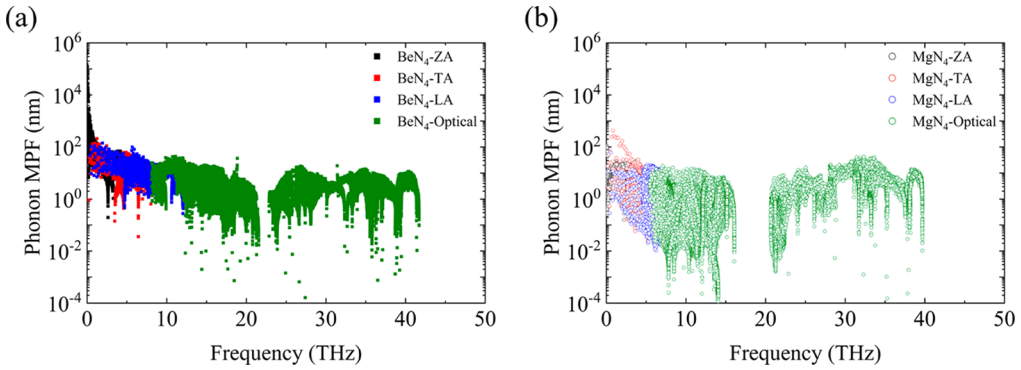

Figure 10. Phonon mean free path (MFP) of (a) BeN_4 and (b) MgN_4 monolayers as a function of frequency at 300 K.

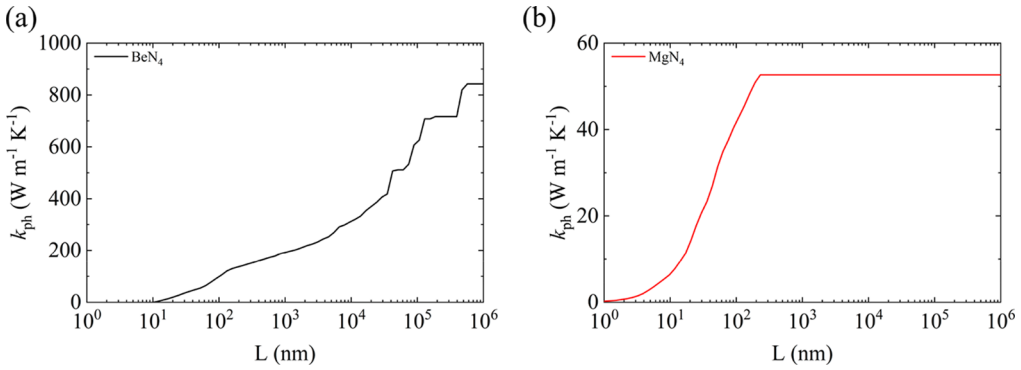

Figure 11. Cumulative thermal conductivities of (a) BeN_4 and (b) MgN_4 monolayers as a function of phonon MFP at 300 K.

lead to a higher lattice thermal conductivity of BeN_4 monolayer. To reveal the phonon anharmonic properties of BeN_4 and MgN_4 monolayers, the MWGP and P_3 are analyzed. The MWGP can describe the strength of the phonon scattering channel, which depends on the anharmonicity of the phonon branch. The MWGP of BeN_4 and MgN_4 monolayers are 2.84 and 5.62, respectively. The larger MWGP means the stronger anharmonicity of the phonon branch, resulting in stronger phonon scattering and lower phonon lifetime.[41] Meanwhile, P_3 will reflect the number of phonon scattering channels, and the larger P_3 indicates stronger phonon scattering. Figure 9 exhibits the P_3 of BeN_4 and MgN_4 monolayers. It can be seen that in the whole frequency region, the P_3 of BeN_4 and MgN_4 monolayers are comparable with each other. The total P_3 of BeN_4 monolayer is 1.94×10^{-3}, which is slightly smaller than that of MgN_4 monolayer (2.07×10^{-3}). The discrepancy of P_3 between BeN_4 and MgN_4 monolayers is negligible, thus the enhancing phonon scattering of MgN_4 monolayer is only ascribed to the strength of the phonon scattering channel. Hence, compared that of to MgN_4 monolayer, the higher lattice thermal conductivity of BeN_4 monolayer can be attributed to the following aspects: (1) the higher phonon heat capacity, (2) the larger phonon group velocity, (3) the longer phonon lifetime due to the stronger phonon scattering.

In addition, the phonon MFP plays a crucial role in phonon thermal transport. We calculate the phonon MFP (l_λ) based on the phonon group velocity and phonon lifetime, that is, $l_\lambda = v_\lambda \tau_\lambda$. As displayed in Figure 10, for BeN_4 monolayer, the phonon MFP generally drops as the frequency increases. The acoustic phonon MFPs of BeN_4 monolayer are larger than those of optical phonon MFPs. Especially, when the frequency is less than 3 THz, the MFP of ZA phonon branch is much higher than those of TA and LA phonon branches. However, for the MgN_4 monolayer, the acoustic phonon MFPs show little deviation from the optical phonon MFPs. At a frequency below 5 THz, the MFP of the ZA phonon branch is 1 order of magnitude higher than those of the other two phonon branches. The average phonon MFPs of BeN_4 and MgN_4 monolayers are 39.30 and 4.25 nm, which demonstrates that BeN_4 monolayer has the higher lattice thermal conductivity. Typically, when the system length is smaller than l_λ, phonon transport belongs to the ballistic regime without scattering. When the system length is larger than l_λ, the phonon moves diffusively with collision. Thus, the cumulative lattice thermal conductivity should be analyzed to exhibit the phonon MFP distribution. The lattice thermal conductivity as a function of phonon MFP can be given by:[42]

$$k_{\mathrm{ph}}(L) = k_{\mathrm{ph}}^{\alpha\alpha}(L) = \sum_{\lambda}^{l_\lambda < L} C_\lambda v_{\lambda\alpha}^2 \tau_{\lambda\alpha} \tag{5}$$

The calculated cumulative lattice thermal conductivities of BeN_4 and MgN_4 monolayers are shown in Figure 11. As the phonon MFP increases, the cumulative lattice thermal conductivities of BeN_4 and MgN_4 monolayers increase until reaching the maximum values, and the corresponding phonon MFP can be defined as the longest phonon MFP (L_{max}). For BeN_4 monolayer, the phonons with large MFP have a significant contribution to lattice thermal conductivity. Nevertheless, the phonons with the small MFP of MgN_4 monolayer dominate lattice thermal conductivity. The L_{max} of BeN_4 monolayer is longer than 10 μm, and the corresponding value of MgN_4 monolayer is smaller than 1 μm, which reveals that the lattice thermal conductivity of BeN_4 monolayer has stronger size effect.

https://doi.org/10.1021/acsomega.2c00785
ACS Omega 2022, 7, 10812−10819

4. CONCLUSIONS

We investigate systematically the thermal properties of MN_4 monolayers using first-principles calculations. The lattice thermal conductivities of BeN_4 and MgN_4 monolayers are anisotropic at 300 K, which are equal to 842.75 (615.97) W m^{-1} K^{-1} and 52.66 (21.76) W m^{-1} K^{-1} along the armchair (zigzag) direction, respectively. The lattice thermal conductivity of BeN_4 monolayer is much larger than that of MgN_4 monolayer. When the temperature rises to 900 K, the corresponding reduction along the armchair zigzag directions are 71.94% and 72.13%, 50.11% and 63.43%, respectively. Meanwhile, the low frequency phonon branches have a major contribution to the total lattice thermal conductivities of BeN_4 and MgN_4 monolayers, which includes acoustic phonon branches and low frequency optical phonon branches. Moreover, the phonon behaviors are investigated, such as phonon heat capacity, phonon group velocity, phonon lifetime, MWGP, P_3, MFP, and cumulative lattice thermal conductivity. For BeN_4 monolayer, the average phonon heat capacity, phonon group velocity, and phonon lifetime are 3.54×10^5 J K^{-1} m^{-3}, 3.61 km s^{-1}, and 13.64 ps. The corresponding values of MgN_4 monolayer are 3.42×10^5 J K^{-1} m^{-3}, 3.27 km s^{-1}, and 1.70 ps, respectively. Hence, we attribute the higher lattice thermal conductivity of BeN_4 monolayer to the larger phonon heat capacity, phonon group velocity, and phonon lifetime. Furthermore, the MWGP and P_3 of BeN_4 monolayer (2.84 and 1.94×10^{-3}) are lower than those of MgN_4 monolayer (5.62 and 2.07×10^{-3}), which reveals that stronger phonon scattering is present in MgN_4 monolayer. Subsequently, the phonon MFPs of BeN_4 and MgN_4 monolayers are evaluated, of which the average values are 39.30 and 4.25 nm, respectively. The cumulative lattice thermal conductivities of two monolayers increase gradually until reaching saturation values with the increasing phonon MFP. The L_{max} of BeN_4 monolayer is much longer than that of MgN_4 monolayer, indicating that the lattice thermal conductivity of BeN_4 monolayer exhibits a stronger size dependence. The study explores the thermal properties of novel 2D Dirac materials MN_4 monolayer, which will contribute to a better understanding of thermal management in 2D MN_4 based nanoelectronic devices.

AUTHOR INFORMATION

Corresponding Author

Dan Han − *College of Electrical, Energy and Power Engineering, Yangzhou University, Yangzhou 225127, China;* orcid.org/0000-0002-0736-4718; Email: han@yzu.edu.cn

Author

Man Wang − *Institute of Thermal Science and Technology, Shandong University, Jinan 250061, China;* orcid.org/0000-0003-3979-287X

Complete contact information is available at: https://pubs.acs.org/10.1021/acsomega.2c00785

Notes

The authors declare no competing financial interest.

REFERENCES

(1) Novoselov, K. S.; Geim, A. K.; Morozov, S. V.; Jiang, D.; Zhang, Y.; Dubonos, S. V.; Grigorieva, I. V.; Firsov, A. A. Electric field effect in atomically thin carbon films. *Science* **2004**, *306* (5696), 666−669.

(2) Bolotin, K. I.; Sikes, K. J.; Jiang, Z.; Klima, M.; Fudenberg, G.; Hone, J.; Kim, P.; Stormer, H. L. Ultrahigh electron mobility in suspended graphene. *Solid State Commun.* **2008**, *146* (9), 351−355.

(3) Zhang, Y.; Tan, Y.-W.; Stormer, H. L.; Kim, P. Experimental observation of the quantum Hall effect and Berry's phase in graphene. *Nature* **2005**, *438* (7065), 201−204.

(4) Bolotin, K. I.; Ghahari, F.; Shulman, M. D.; Stormer, H. L.; Kim, P. Observation of the fractional quantum Hall effect in graphene. *Nature* **2009**, *462* (7270), 196−199.

(5) Ponomarenko, L. A.; Gorbachev, R. V.; Yu, G. L.; Elias, D. C.; Jalil, R.; Patel, A. A.; Mishchenko, A.; Mayorov, A. S.; Woods, C. R.; Wallbank, J. R.; Mucha-Kruczynski, M.; Piot, B. A.; Potemski, M.; Grigorieva, I. V.; Novoselov, K. S.; Guinea, F.; Fal'ko, V. I.; Geim, A. K. Cloning of Dirac fermions in graphene superlattices. *Nature* **2013**, *497* (7451), 594−597.

(6) Han, D.; Fan, H.; Wang, X.; Cheng, L. Atomistic simulations of phonon behaviors in isotopically doped graphene with Sierpinski carpet fractal structure. *Mater. Res. Express* **2020**, *7* (3), 035020.

(7) Liu, C.; Lu, P.; Chen, W.; Zhao, Y.; Chen, Y. Phonon transport in graphene based materials. *Phys. Chem. Chem. Phys.* **2021**, *23* (46), 26030−26060.

(8) Han, D.; Wang, X.; Ding, W.; Chen, Y.; Zhang, J.; Xin, G.; Cheng, L. Phonon thermal conduction in a graphene−C_3N heterobilayer using molecular dynamics simulations. *Nanotechnology* **2019**, *30* (7), 075403.

(9) Lee, C.; Wei, X.; Kysar, J. W.; Hone, J. Measurement of the elastic properties and intrinsic strength of monolayer graphene. *Science* **2008**, *321* (5887), 385−388.

(10) Castro Neto, A. H.; Guinea, F.; Peres, N. M. R.; Novoselov, K. S.; Geim, A. K. The electronic properties of graphene. *Rev. Mod. Phys.* **2009**, *81* (1), 109−162.

(11) Tan, C.; Cao, X.; Wu, X.-J.; He, Q.; Yang, J.; Zhang, X.; Chen, J.; Zhao, W.; Han, S.; Nam, G.-H.; Sindoro, M.; Zhang, H. Recent Advances in Ultrathin Two-Dimensional Nanomaterials. *Chem. Rev.* **2017**, *117* (9), 6225−6331.

(12) Zhang, H. Ultrathin Two-Dimensional Nanomaterials. *ACS Nano* **2015**, *9* (10), 9451−9469.

(13) Liu, C.-C.; Jiang, H.; Yao, Y. Low-energy effective Hamiltonian involving spin-orbit coupling in silicene and two-dimensional germanium and tin. *Phys. Rev. B* **2011**, *84* (19), 195430.

(14) Cai, B.; Zhang, S.; Hu, Z.; Hu, Y.; Zou, Y.; Zeng, H. Tinene: a two-dimensional Dirac material with a 72 meV band gap. *Phys. Chem. Chem. Phys.* **2015**, *17* (19), 12634−12638.

(15) Wang, J.; Deng, S.; Liu, Z.; Liu, Z. The rare two-dimensional materials with Dirac cones. *Natl. Sci. Rev.* **2015**, *2* (1), 22−39.

(16) Young, S. M.; Wieder, B. J. Filling-Enforced Magnetic Dirac Semimetals in Two Dimensions. *Phys. Rev. Lett.* **2017**, *118* (18), 186401.

(17) Qi, M.; An, C.; Zhou, Y.; Wu, H.; Zhang, B.; Chen, C.; Yuan, Y.; Wang, S.; Zhou, Y.; Chen, X.; Zhang, R.; Yang, Z. Pressure-driven Lifshitz transition in type-II Dirac semimetal $NiTe_2$. *Phys. Rev. B* **2020**, *101* (11), 115124.

(18) Bykov, M.; Fedotenko, T.; Chariton, S.; Laniel, D.; Glazyrin, K.; Hanfland, M.; Smith, J. S.; Prakapenka, V. B.; Mahmood, M. F.; Goncharov, A. F.; Ponomareva, A. V.; Tasnádi, F.; Abrikosov, A. I.; Bin Masood, T.; Hotz, I.; Rudenko, A. N.; Katsnelson, M. I.; Dubrovinskaia, N.; Dubrovinsky, L.; Abrikosov, I. A. High-pressure synthesis of Dirac materials: layered van der Waals bonded BeN_4 polymorph. *Phys. Rev. Lett.* **2021**, *126* (17), 175501.

(19) Mortazavi, B.; Shojaei, F.; Zhuang, X. Ultrahigh stiffness and anisotropic Dirac cones in BeN_4 and MgN_4 monolayers: a first-principles study. *Mater. Today Nano* **2021**, *15*, 100125.

(20) Tong, Z.; Pecchia, A.; Yam, C.; Bao, H.; Dumitrică, T.; Frauenheim, T. Significant Increase of Electron Thermal Conductivity in Dirac Semimetal Beryllonitrene by Doping Beyond Van Hove Singularity. *Adv. Funct. Mater.* **2022**, 2111556.

(21) Kresse, G.; Furthmüller, J. Efficient iterative schemes for ab initio total-energy calculations using a plane-wave basis set. *Phys. Rev. B* **1996**, *54* (16), 11169−11186.

(22) Perdew, J. P.; Burke, K.; Ernzerhof, M. Generalized gradient approximation made simple. *Phys. Rev. Lett.* **1996**, *77* (18), 3865−3868.
(23) Li, W.; Carrete, J.; A. Katcho, N.; Mingo, N. ShengBTE: a solver of the Boltzmann transport equation for phonons. *Comput. Phys. Commun.* **2014**, *185* (6), 1747−1758.
(24) Gao, Z.; Zhu, T.; Sun, K.; Wang, J.-S. Highly Anisotropic Thermoelectric Properties of Two-Dimensional As_2Te_3. *ACS Appl. Electron. Ma.* **2021**, *3* (4), 1610−1620.
(25) Han, D.; Yang, X.; Du, M.; Xin, G.; Zhang, J.; Wang, X.; Cheng, L. Improved thermoelectric properties of WS_2−WSe_2 phononic crystals: insights from first-principles calculations. *Nanoscale* **2021**, *13* (15), 7176−7192.
(26) Yang, X.; Han, D.; Wang, M.; Du, M.; Wang, X. Extraordinary thermoelectric performance in 2D group □ monolayer XP_3 (X = Al, Ga, and In). *J. Phys. D Appl. Phys.* **2021**, *54*, 435501.
(27) Yuan, K.; Zhang, X.; Li, L.; Tang, D. Effects of tensile strain and finite size on thermal conductivity in monolayer WSe_2. *Phys. Chem. Chem. Phys.* **2019**, *21* (1), 468−477.
(28) Baroni, S.; De Gironcoli, S.; Dal Corso, A.; Giannozzi, P. Phonons and related crystal properties from density-functional perturbation theory. *Rev. Mod. Phys.* **2001**, *73* (2), 515−562.
(29) Togo, A.; Oba, F.; Tanaka, I. First-principles calculations of the ferroelastic transition between rutile-type and $CaCl_2$-type SiO_2 at high pressures. *Phys. Rev. B* **2008**, *78* (13), 134106.
(30) Bafekry, A.; Stampfl, C.; Faraji, M.; Yagmurcukardes, M.; Fadlallah, M. M.; Jappor, H. R.; Ghergherehchi, M.; Feghhi, S. A. H. A Dirac-semimetal two-dimensional BeN4: thickness-dependent electronic and optical properties. *Appl. Phys. Lett.* **2021**, *118* (20), 203103.
(31) Guan, J.; Zhu, Z.; Tománek, D. Phase coexistence and metal-insulator transition in few-layer phosphorene: a computational study. *Phys. Rev. Lett.* **2014**, *113* (4), 046804.
(32) Yao, S.; Zhang, X.; Zhang, Z.; Chen, A.; Zhou, Z. 2D Triphosphides: SbP_3 and GaP_3 monolayer as promising photocatalysts for water splitting. *Int. J. Hydrogen Energy* **2019**, *44* (12), 5948−5954.
(33) Han, D.; Ding, W.; Wang, X.; Cheng, L. Tunable thermal transport in a WS_2 monolayer with isotopic doping and fractal structure. *Nanoscale* **2019**, *11* (42), 19763−19771.
(34) Sun, Z.; Yuan, K.; Chang, Z.; Bi, S.; Zhang, X.; Tang, D. Ultra-low thermal conductivity and high thermoelectric performance of two-dimensional triphosphides (InP_3, GaP_3, SbP_3 and SnP_3): a comprehensive first-principles study. *Nanoscale* **2020**, *12* (5), 3330−3342.
(35) Ouyang, T.; Jiang, E.; Tang, C.; Li, J.; He, C.; Zhong, J. Thermal and thermoelectric properties of monolayer indium triphosphide (InP_3): a first-principles study. *J. Mater. Chem. A* **2018**, *6* (43), 21532−21541.
(36) Gupta, N.; Verma, R. First-principles study of thermoelectric transport properties in low-buckled monolayer silicene. *Physica B* **2021**, *606*, 412715.
(37) Hu, Y.; Yang, T.; Li, D.; Ding, G.; Dun, C.; Wu, D.; Wang, X. Origins of minimized lattice thermal conductivity and enhanced thermoelectric performance in WS_2/WSe_2 lateral superlattice. *ACS Omega* **2021**, *6* (11), 7879−7886.
(38) Mobaraki, A.; Kandemir, A.; Yapicioglu, H.; Gülseren, O.; Sevik, C. Validation of inter-atomic potential for WS_2 and WSe_2 crystals through assessment of thermal transport properties. *Comput. Mater. Sci.* **2018**, *144*, 92−98.
(39) Yang, X.; Han, D.; Fan, H.; Wang, M.; Du, M.; Wang, X. First-principles calculations of phonon behaviors in graphether: a comparative study with graphene. *Phys. Chem. Chem. Phys.* **2021**, *23* (1), 123−130.
(40) Han, D.; Sun, H.; Ding, W.; Chen, Y.; Wang, X.; Cheng, L. Effect of biaxial strain on thermal transport in WS_2 monolayer from first principles calculations. *Physica E* **2020**, *124*, 114312.
(41) Peng, B.; Zhang, H.; Shao, H.; Xu, Y.; Ni, G.; Zhang, R.; Zhu, H. Phonon transport properties of two-dimensional group-IV materials from ab initio calculations. *Phys. Rev. B* **2016**, *94* (24), 245420.
(42) Peng, B.; Zhang, H.; Shao, H.; Xu, Y.; Zhang, X.; Zhu, H. Towards intrinsic phonon transport in single-layer MoS_2. *Ann. Phys.* **2016**, *528* (6), 504−511.

https://doi.org/10.1021/acsomega.2c00785
ACS Omega 2022, 7, 10812−10819